Magnet-assisted electrochemical immunosensor based on surface-clean Pd-Au nanosheets for sensitive detection of SARS-CoV-2 spike protein

Jialin Zhao [a,b,§], Zhao Fu [a,§], Haolin Li [a,b], Youlin Xiong [a], Shuangfei Cai [a], Chen Wang [a], Yunfa Chen [c], Ning Han [c], Rong Yang [a,b,*]

[a] *CAS Key Laboratory for Biomedical Effects of Nanomaterials and Nanosafety, Center of Materials Science and Optoelectronics Engineering, CAS Center for Excellence in Nanoscience, National Center for Nanoscience and Technology, University of Chinese Academy of Sciences, No.11 ZhongGuanCun BeiYiTiao, Beijing 100190, China*

[b] *Sino-Danish College, Sino-Danish Center for Education and Research, University of Chinese Academy of Sciences, Beijing 100049, China*

[c] *State Key Laboratory of Multiphase Complex Systems, Institute of Process Engineering, Chinese Academy of Sciences, Beijing, China*

ARTICLE INFO

ABSTRACT

Tracking and monitoring of low concentrations of severe acute respiratory syndrome coronavirus 2 (SARS-CoV-2) can effectively control asymptomatic transmission of current coronavirus disease 2019 (COVID-19) in the early stages of infection. Here, we highlight an electrochemical immunosensor for sensitive detection of SARS-CoV-2 antigen marker spike protein. The surface-clean Pd-Au nanosheets as a substrate for efficient sensing and signal output have been synthesized. The morphology, chemical states and excellent stable electrochemical properties of this surface-clean heterostructures have been studied. Functionalized superparamagnetic nanoparticles (MNPs) were introduced as sample separators and signal amplifiers. This biosensor was tested in phosphate buffered saline (PBS) and nasopharyngeal samples. The results showed that the sensor has a wide linear dynamic range (0.01 ng mL^{-1} to 1000 ng mL^{-1}) with a low detection limit (0.0072 ng mL^{-1}), which achieved stable and sensitive detection of the spike protein. Therefore, this immunosensing method provides a promising electrochemical measurement tool, which can furnish ideas for early screening and the reasonable optimization of detection methods of SARS-CoV-2.

1. Introduction

The coronavirus disease 2019 (COVID-19) outbreak has brought an unprecedented devastating impact on human life around the world [1,2]. Until September 2021, the number of people infected with the virus has exceeded 220 million and continues to rise [3]. These days the SARS-CoV-2 virus, which can cause various degrees of upper respiratory disease, has been deeply analyzed [4–9]. The β-coronavirus is a sequence of RNA genome with single-positive strand characteristics. It mainly encodes four structural proteins, including small envelope (E) protein, nucleocapsid (N) protein, spike (S) protein and matrix (M) protein [10,11]. The infection route of SARS-CoV-2 can be achieved through a variety of contact or non-contact ways, and no obvious clinical symptoms appear in the early stage [12,13]. Therefore, rapid virus screening can al-leviate the fatal flaws of asymptomatic transmission that appeared in this pandemic.

At present, the detection of SARS-CoV-2 in the public health system is mainly through the PCR method targeting RNA and the ELISA method targeting antibody [14–17]. However, the PCR method takes a long time, especially for such a large infection base; and the antibody detection technology of ELISA is not suitable for early screening of COVID-19, but is more conducive to the recovery period after treatment [1]. Therefore, more and more attention is focused on the antigen coexisting in the virus as a potential detection target [18]. Among a variety of predicted antigenic biomarkers, the S protein that mediates adhesion to host cells has been reported to be one of the most valuable detection targets [9,19]. S1 protein with receptor binding domain (RBD) located on the surface of the virus generally recognizes and binds to host cells, contributing to the development of clinical diagnostic kits suitable for sensitive detection in the field [20]. Therefore, the design and development of practical methods for tracking and detection S1 protein in respiratory samples are extremely important.

---

* Corresponding author
E-mail address: yangr@nanoctr.cn (R. Yang).
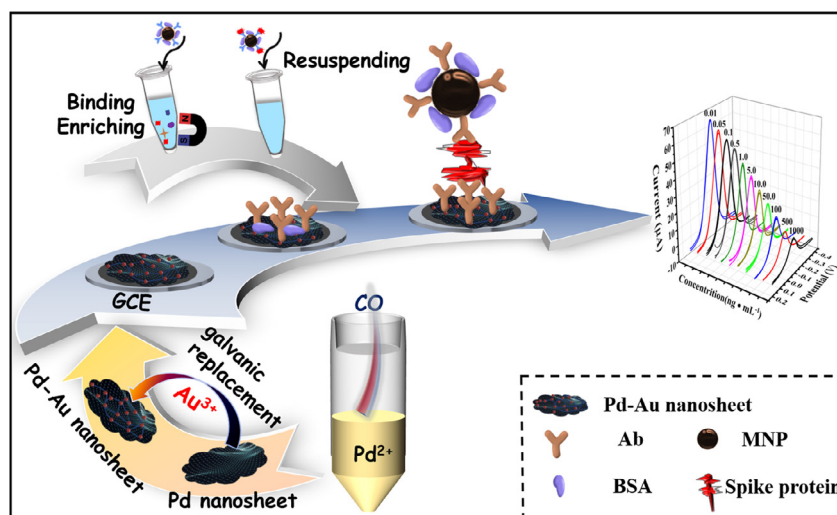§ J.L. Zhao and Z. Fu contributed equally to this work.

Fig. 1. Schematic illustration of the magnet-assisted electrochemical immunosensor based on Pd-Au nanosheets.

Electrochemical sensors that can convert changes in active biological substrates into capturable electrical signals have predictable potential [21–23]. The electrochemical detection method exhibits the advantages of high sensitivity and simple processing, and it is very promising to construct methods such as remote controllable measurement or on-site instant detection driven by a smartphone [24,25]. The layered noble metal nanocomposite has high conductivity, large surface area and flexibly adjustable surface chemistry [26]. Among them, thin-layer metal nanosheets formed by embedding or converting other metal ions can provide many possibilities for the desired design and function. However, most thin-layer multi-metal nanosheets need to introduce a large amount of surfactants and stabilizers during the preparation process, and accompanied by harsh synthesis conditions, which greatly block their active sites and reduce their inherent activity. So far, simple preparation methods of layered bimetallic nanosheets with surface-clean heterostructures are quite rare. As a sensing substrate, the enhanced electrocatalytic performance by the synergistic effect and high chemical stability make it undoubtedly have important capabilities in the field of electrochemical measurement [27,28]. In the constructed antigen-based sensor, the introduction of high charge concentration and appropriate electron mobility can promote the transfer of electrons from biomolecules to the sensor platform, enabling the detection of ultra-low levels of biological species [25].

Magnetic nanoparticles (MNPs) have advantages in virus detection, especially in this COVID-19 pandemic [29–31]. Magnetic labels can meet the requirements of rapid separation and enrichment, and low cost-effectiveness [32]. Although the magnetic properties of MNP have been extensively studied, the employment of MNP is obviously more direct and effective in rapid and sensitive screening such as SARS-CoV-2. MNPs can reduce the amount of sample processing while simplifying the method, and can also exert its signal amplification function in electrochemical biosensing.

Here, we designed a magnet-assisted electrochemical immunosensor based on Pd-Au nanosheets for sensitive detection of S1 protein (Fig. 1). Pd-Au nanosheets are selected as the sensing and fixing substrate. The surface-clean Pd precursor is used as the sacrificial template. It is worth mentioned that the entire preparation system was carried out at room temperature without any surface agents or stabilizers. The excellent conductivity and large surface area greatly enhanced the electronic transport and signal output between the interface and the solution. Antibody-functionalized MNPs were introduced as sample separators and

signal amplifiers. The results showed a wide linear range (0.01 ng mL^{-1} to 1000 ng mL^{-1}) and an ultra-low detection limit (LOD, 0.0072 ng mL^{-1}), which achieved stable and sensitive detection of the S protein. This is essential for the initial monitoring of the virus. Meanwhile, this electrochemical immunosensor showed good selectivity, repeatability and stability. Overall, the successful casting of electrochemical biosensors combining Pd-Au nanosheets and functionalized MNPs provides a valuable analysis and application approach for antigen detection.

2. Experimental section

2.1. Materials and apparatuses

HAuCl$_4$•3H$_2$O, Palladium(II) 2,4-pentanedionate (Pd(acac)$_2$), Fe(NO$_3$)$_3$•9H$_2$O, hemin, bovine serum albumin (BSA), citric acid, ascorbic acid (AA), sodium acetate anhydrous and urea (UA) were purchased from Alfa Aesar Co., Ltd. (Beijing, China). 1-ethyl-3-(3-dimethylaminopropyl) carbodiimide hydrochloride (EDC) and N-hydroxysulfosuccinimide (NHS) were received from Innochem Co., Ltd. (Beijing, China). Glacial acetic acid and ethylene glycol were supplied by Beijing Chemical Inductry Groups Co., Ltd. (China). D-(+)-glucose, AgNO$_3$ and glucose oxidase (Gox) were obtained from Sigma-Aldrich (Shanghai, China). H$_2$O$_2$ was obtained from Acros Organics (USA). SARS-CoV-2 S1 recombinant protein (S1 protein), nucleocapsid protein (N protein) and anti-SARS-CoV S1 antibody (Ab) were purchased from Sangon Biotech Co., Ltd. (Shanghai, China). All aqueous solutions were made using ultrapure 18.2 MΩ cm water.

Scanning electron microscope (SEM, Hitachi-SU8220, Japan) and transmission electron microscope (TEM, Tecnai G2 F20 U-TWIN, USA) were used to characterize the morphology of Pd-Au nanosheets. The surface modification of MNPs was identified by fourier transform infrared spectroscopy (FT-IR, Spectrum One, USA). The potential measurement was carried out by the Zetasizer instrument (Zetasizer Nano ZS, England). The crystal structures of nanomaterials were studied by X-ray powder diffraction (XRD, M18XHF, Japan). The chemical elements and structure of the nanosheets were analyzed by X-ray photoelectron spectroscopy (XPS, ESCALAB 250Xi, England). All electrochemical measurements were recorded by Chenhua Electrochemical Instrument (CHI 660, China). The typical three-electrode system used includes counter electrode (platinum electrode), reference electrode (saturated calomel electrode) and working electrode.

2.2. Preparation of Pd-Au nanosheet

The precursor Pd nanosheets were synthesized with modification according to the previously reported method [33]. First, 15.2 mg of Pd(acac)$_2$ was ultrasonic dissolved in 10 mL of glacial acetic acid. Then, CO gas was introduced into the mixed solution at a flow rate of 250 mL min^{-1} and maintained for 30 min; after that, the above reaction solution was sealed and allowed to stand for 24 h During this process, the color of the solution changed from yellow to black, and Pd nanosheets gradually formed and settled slowly. Finally, the products were washed thoroughly with ethanol and re-dispersed in ultrapure water.

Pd-Au composite nanosheets were synthesized by a simple method of galvanic replacement without the use of additional reductants. First, 10 mL of ultrasonically dispersed Pd sheets was transferred to a flask and stirred vigorously, and then an aqueous solution containing 4 mL of 26.32 mM HAuCl$_4$•3H$_2$O was dropped into the flask at a flow rate of 33.3 mL min^{-1} using an auto-injector. Then the reaction system continued to stir for 1 h to fully carry out the displacement reaction. Finally, Pd-Au nanosheets were obtained by washing several times with ultrapure water.

2.3. Synthesis and modification of MNP

The typical synthesis of MNPs was performed as previously reported [34]. In short, MNPs with core-shell structure were prepared by a simple solvothermal method. First, Fe(NO$_3$)$_3$•9H$_2$O, anhydrous sodium acetate and AgNO$_3$ were fully dissolved in the ethylene glycol solution, and then the mixture was transferred to an autoclave and reacted at 210°C for 4 h After cooling, it was magnetically separated and thoroughly washed with ethanol and ultrapure water. Then, citric acid was added to the prepared MNPs solution to improve the stability of the MNP colloidal solution. Finally, the stable citrate-coated MNP was obtained. See the details about the preparation of MNP and functionalization in Supporting Information.

2.4. Modification of immunosensing electrode

The glassy carbon electrode (GCE) was pretreated according to our previous procedure [35,36]. Next, 20 μL of 1 mg mL^{-1} Pd-Au nanosheets was cast on the surface of the GCE and dried at 40°C. The modified electrode was immersed in 10 mM PBS solution and used for further experiments. Then, 15 μg mL^{-1} S1 protein antibody was irradiated with UV light of 300 mW/cm^2 for 30 s to generate sulfhydryl groups for immobilization. This process relies on simple and mature photochemical immobilization technology [37,38]. After that, 10 μL S1 protein antibody was used to incubate the electrode chip for 1 h under 25°C and blocked with 0.1 mg mL^{-1} BSA solution to avoid possible nonspecific adsorption. At the same time, 50 μL 1.0 μg mL^{-1} antibody-modified MNPs was mixed with the same volume of the sample to be analyzed and incubated in a 37°C shaker for 40 min, then magnetically separated and re-dispersed in 50 μL PBS. Finally, the formed MNPs-Ab-S1 were reacted and bound with the antibody on the interface for 40 min, then washed with PBS and used for measurement next.

2.5. Sample assay and electrochemical measurements

Nasopharyngeal samples were collected using sterile swab sticks and invaded into 2.5 mL PBS. After standing for 1 h, the samples were centrifuged and diluted twice as a stock solution for the dilution of spike protein. Then, 1 mg mL^{-1} spike protein was successively diluted with stock solution and stored at 4°C for later use.

All the electrochemical measurements are carried out using a standard three-electrode system. The differential pulse voltammetry (DPV) and cyclic voltammetry (CV) programs are executed in 0.01 M PBS containing 10 mM H$_2$O$_2$. The CV potential scanning range is 0.8 V $\sim$ −0.8 V, 0.6 V $\sim$ −0.6 V and 0.6 V $\sim$ −0.3 V; DPV scanning range is 0.2 V $\sim$ −0.4 V; the scanning rate of the amperometric measurement above is 50 mV s^{-1}. The electrochemical impedance spectroscopy (EIS) measurement is performed employing a series of 0.005 V amplitude sinusoidal waveforms from 0.1 Hz to 100,000 Hz in 5 mM [Fe(CN)$_6$]$^{3-/4-}$ solution in 0.01 M PBS.

3. Results and discussion

3.1. Characterization of Pd-Au nanosheets

The microstructure and surface morphology of the Pd-Au nanosheets were characterized by TEM and SEM. The TEM images revealed the thin-layer structure of Pd-Au hybrid nanosheets (Fig. 2A, 2B and Fig. S1). In the high-resolution TEM image (Fig. 2C); the lattice spacing of Pd was 0.221 nm, while the gold nanostructure showed a larger lattice spacing of 0.235 nm, which was consistent with the face-centered cubic structure (111) of Au [34,39]. The SEM images (Fig. 2D, 2E and Fig. S2) described the overall morphology of Pd-Au nanosheets, which were flower-like thin-layer structures with large surface areas. The EDS mapping images exhibited that Pd and Au coexist in Pd-Au nanosheets (Fig. 2F and Fig. S3), and the Pd element was significantly higher than Au; while the Pd nanosheet only showed Pd element and strong Si element, which was attributed to the SiO$_2$ film (Fig. S4). XPS survey spectrum was used to further analyze the chemical elements and existing states of Pd-Au nanocomposite. Fig. 2G and Fig. S5 revealed the overall survey and individual XPS element scan results. In the Pd 3d spectrum, Pd 3d$_{3/2}$ and Pd 3d$_{5/2}$ pertained to the peaks at 340.3 and 335.0 eV respectively, while the peaks at 335.8 and 341.2 eV were attributed to Pd^{2+} (Fig. S5A). The 87.3 and 83.6 eV peaks of Au were located in Au 4f$_{5/2}$ and Au 4f$_{7/2}$ (Fig. S5B) [40]. The peaks of C 1s and O 1s were revealed at 284.8, 285.9 and 532.0 eV (Fig. S5C, S5D), respectively, which originated from CO and glacial acetic acid in simple synthesis [41]. The crystal structure of the synthesized material was further explored by XRD. As shown in Figure 1H, the diffraction peaks of the Pd nanosheets were observed at 2θ = 40.12°, 46.66°, 68.12°, 82.10° and 86.62°, respectively, consistent with (111), (200), (220), (311) and (222) planes of the face-centered cubic (fcc) Pd (JCPDS no. 04–0487). Similar observation was obtained from the diffraction peaks of Pd in the Pd-Au nanosheets. Meanwhile, the diffraction peaks of Au (38.28°, 44.80°, 64.68°, 78.93°) could also be matched well with (111), (200), (220) and (311) planes of the fcc Au (JCPDS no. 03–065–2870), respectively. The results suggest that the separation phase of metals existed in the Pd-Au nanosheets.

### 3.2. Characterization and functionalization of MNPs

First, TEM was employed to study the morphology of the MNP. Fig. 3A and 3B showed a relatively uniform MNP of 170 nm, consisting of a dark Ag core and a dense Fe$_3$O$_4$ shell. MNPs exhibited excellent uniformity and dispersion before applied magnet. Rapid separation of MNPs can be completed within 35s after the addition of magnetic field, showing excellent magnetic properties (Fig. 3C). Then, FT-IR spectroscopy (Fig. 3D) and Zeta potential measurement (Fig. 3E) were performed to confirm the MNPs modified by Ab, the infrared radiation results of MNPs-Ab revealed the C = O bond at 1644 cm^{-1} and strong tensile vibrations of the N−H bond at 3446 cm^{-1}, which proved the formation of amide bond. The coupling of MNP and Ab resulted in a change in Zeta potential from −20.2 mV
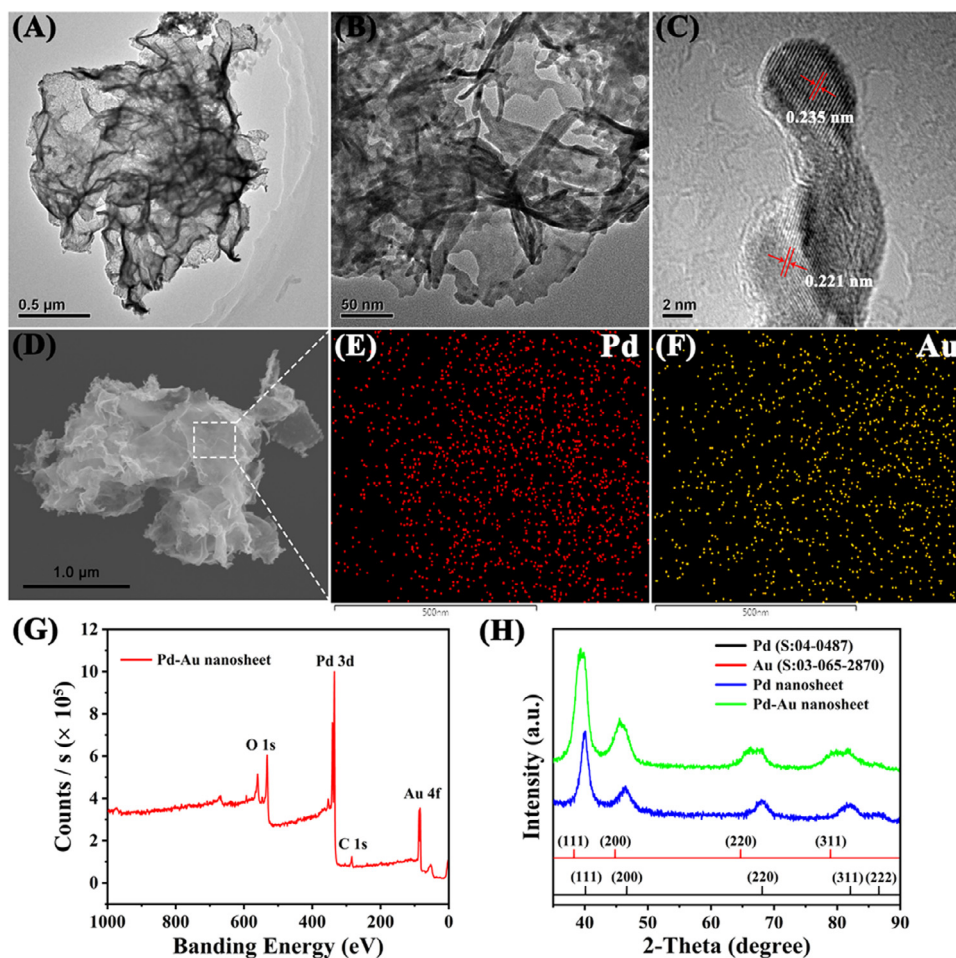
Fig. 2. Characterization of Pd-Au nanosheets. (A) and (B) TEM, (C) HRTEM, (D) SEM, (E) and (F) Corresponding EDX mapping images, (G) XPS survey spectrum, (H) XRD patterns of Pd nanosheets and Pd-Au nanosheets.
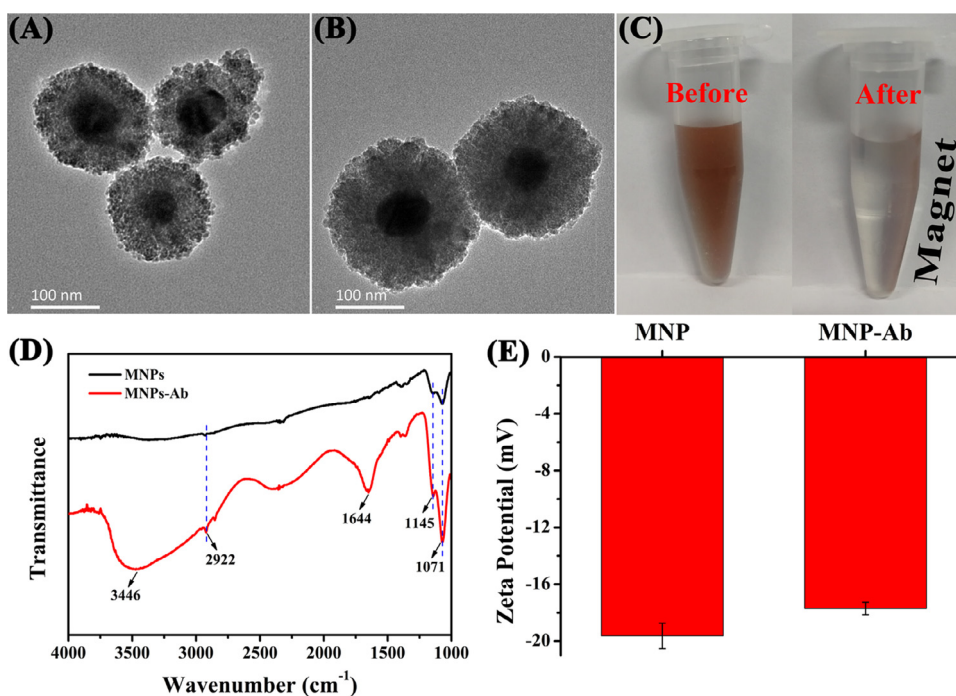
Fig. 3. (A) and (B) TEM images of MNPs. (C) The pictures of MNPs in water before and after magnetic separation. (D) and (E) represent FT-IR spectroscopies and Zeta potentials before and after Ab modification of MNPs, respectively.
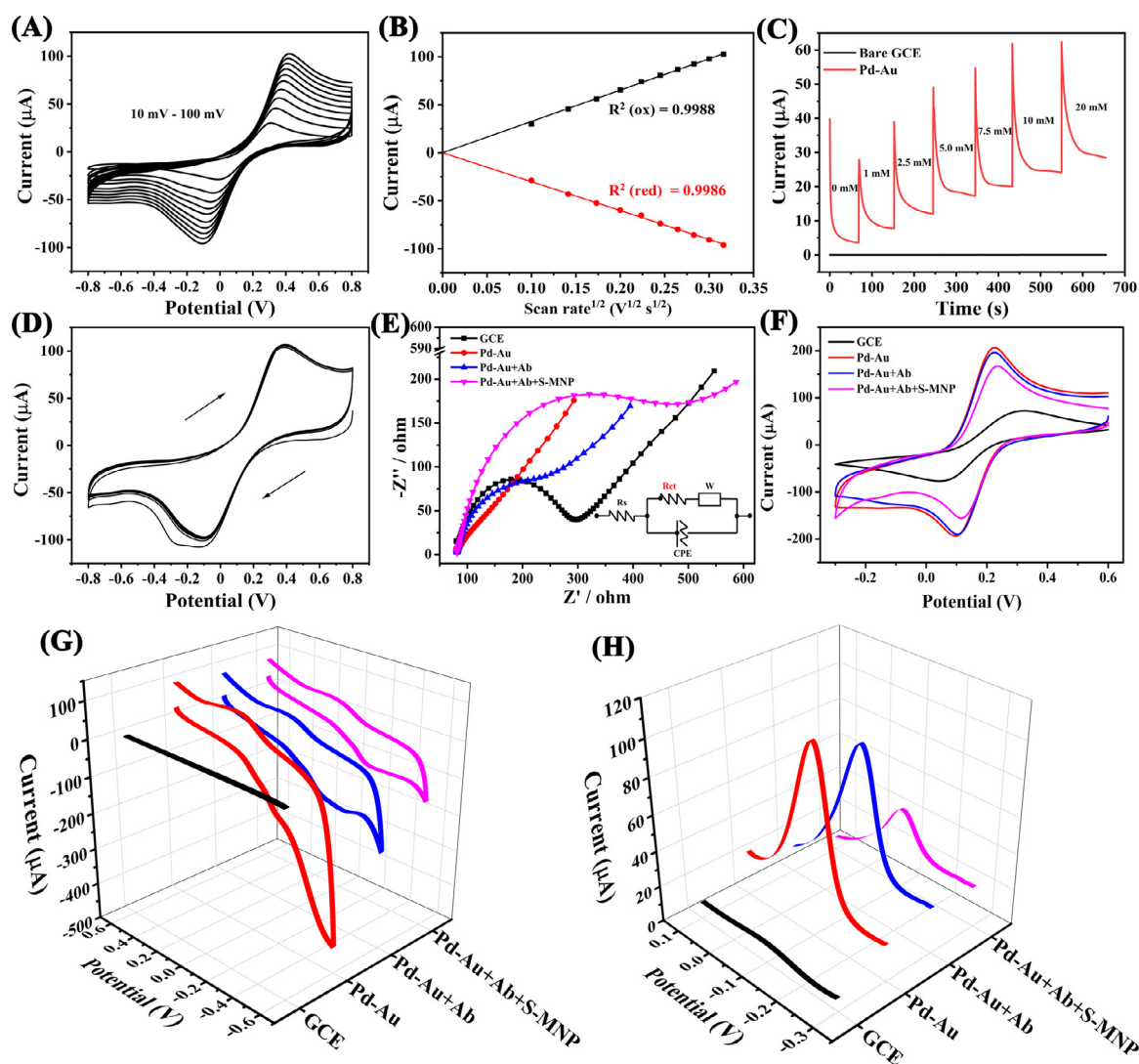
Fig. 4. (A) CV response of Pd-Au nanosheet modified GCE at different scanning rates. (B) The relationship between the square root of the scanning rate and the current. (C) I-t curve of modified electrode in different concentration of H_2O_2 (0 - 20 mM). (D) CV curve of Pd-Au modified GCE after scanning 30 times in 0.01 M PBS containing 5 mM $[Fe(CN)_6]^{3-/4-}$. (E) EIS and CV (F) curves of different modified electrodes in 0.01 M PBS containing 5 mM $[Fe(CN)_6]^{3-/4-}$, respectively. Insert: A modified Randles equivalent circuit for fitting impedance data. R_{ct} represents the charge-transfer resistance, CPE the double-layer capacitance and R_S the resistance of the electrolyte, respectively. W represents the Warburg impendance to describe the low-frequency diffusion process. (G) CV and DPV (H) curves of different modified electrodes in the 10 mM PBS solution containing 10 mM H_2O_2, respectively. DPV amplitude (V): 0.05; pulse width (sec): 0.05; pulse period (sec): 0.5.

to −17.5 mV. The above results indicated the successful modification of Ab on the surface of MNP. Finally, the purified S1 protein and Ab were analyzed by Western Blotting (Fig. S6). The results showed that S1 antigen had strong binding to the Ab.

3.3. Performance evaluation of Pd-Au nanosheets

Here we evaluated the application ability of Pd-Au nanosheets as substrates in electrochemical sensing. First, the CV response was measured at different scanning rates (10 mV s^{-1} - 100 mV s^{-1}) in 5 mM $[Fe(CN)_6]^{3-/4-}$ solution (Fig. 4A), the oxidation and reduction peak currents increased with the increase of scanning rate. There was a good linear relationship between the peak current and the square root of the scanning rate (R^2 (Ox) = 0.9988, R^2 (red) = 0.9986), as shown in Fig. 4B, indicating that the electron transfer in $[Fe(CN)_6]^{3-/4-}$ was reversible and the reaction was a diffusion controlled process [42,43]. The diffusion coefficient calculated by the Randles-Sevcik equation was 6.77×10^{-6} cm^2/s, which was comparable to the previous reports [44–46]. After that, the catalase activity of Pd-Au nanosheets was identified by a sim-

ple visual method (Fig. S7). In the PBS solution containing H_2O_2, a large number of visible bubbles were generated after adding Pd-Au nanosheet in a short time, showing the production of O_2. This result revealed that Pd-Au nanosheets have excellent catalase activity. The formation of precursor Pd nanosheets, the in-situ reduction of Pd and Au^{3+} replacement reactions, and the effective catalysis of the substrate are as follows:

$$Pd^{2+} + 2e^- \xrightarrow{CO} Pd \tag{1}$$

$$3Pd + 2Au^{3+} \rightarrow 3Pd^{2+} + 2Au \tag{2}$$

$$H_2O_2 \xrightarrow{Pd-Au} O_2 + 2H^+ + 2e^- \tag{3}$$

Then, the catalytic ability of Pd-Au nanosheets to substrate H_2O_2 was tested by i-t method (Fig. 4C). The modified electrode showed a step-up current response in different concentrations of H_2O_2 (0 - 20 mM), proving the highly efficient catalytic ability for H_2O_2. In addition, the stability of the nanomaterials was studied (Fig. 4D). The volt-ampere curve was stable after 30 times of CV
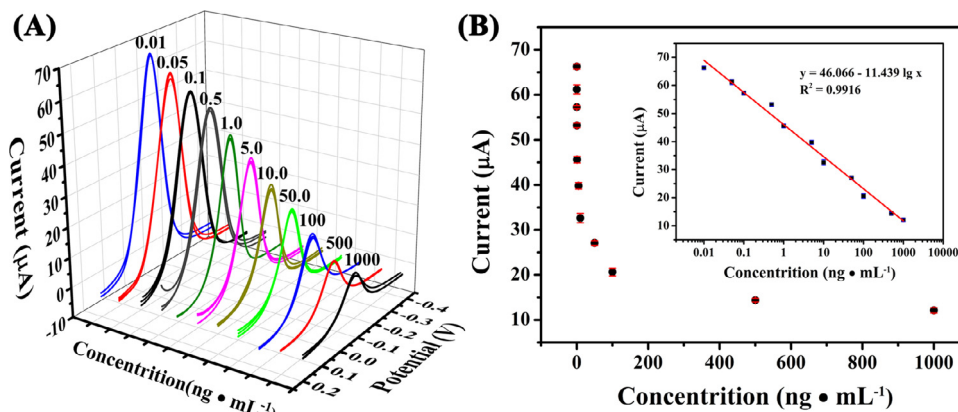
Fig. 5. (A) DPV response curve caused by different concentration of S1 protein ($n = 3$). (B) The relationship between S1 protein concentration and DPV peak current. Inset: Plot of current *vs* logarithm of S1 protein concentration.

scanning, demonstrating that the substrate Pd-Au nanosheets have good stability.

3.4. Electrochemical properties of modified electrode and feasibility

The electrochemical properties of the modified interface were studied by EIS and CV (Fig. 4E and 4F). According to the modification procedure, compared with bare GCE, the load of Pd-Au nanosheets caused a decrease ($\triangle R_{ct} = 198$ Ω) in the diameter of the Nyquist plots (R_{ct} value), the increase of the CV peak current and a lower peak potential separation value ($\triangle Ep$), showing that this process greatly enhanced the electron transport between the interface and the solution. This is due to the large surface area of the Pd-Au nanosheets, which increased the contact and penetration sensitivity of $[Fe(CN)_6]^{3-/4-}$. The modification of antibody and BSA as a blocking agent resulted in an increase ($\triangle R_{ct} = 107$ Ω) in Rct and a decrease in CV peak current, indicating that this process hindered the reversible delivery of the redox probe [35,41]. However, the process exhibited lower spikes. This result can be attributed to the electronic coupling of the reduced probe $[Fe(CN)_6]^{3-}$ with negatively charged proteins (spike protein, BSA and antibody) in cathodic scanning and the greater polarization effect [47,48]. The binding of MNP-Ab-S1 nanocomposite on the surface of GCE further strengthened the above process. These results proved the effectiveness of the construction method. In addition, CV and DPV procedures were performed in PBS solution containing 10 mM H_2O_2 to verify the feasibility of this strategy (Fig. 4G and 4H). The results revealed that the modified Ab showed a reduced current response relative to the Pd-Au nanosheets, and the DPV curve collected the reduction current of H_2O_2 at −0.074 mV. After the MNP-Ab was bound to the target S1 protein, the modified electrode measured the reduced CV and DPV signals. This was because of the MNP, which was a poor conductor and hindered the contact and reaction of Pd-Au nanosheets with H_2O_2 in the solution. Furthermore, the surface morphology of the interface of the modified MNPs-Ab-S1 was characterized by SEM, as shown in Fig. S8. Compared with that one before modification (Fig. S8A-C), the interface after modification of MNPs-Ab-S1 showed that the nanocomposite was bound to the surface of the 3D Pd-Au nanosheet substrate (Fig. S8D-F), indicating the successful capture of S protein by MNP and the effective connection of the nanocomposite to the interface Ab. In general, all test procedures have confirmed the feasibility of this construction strategy.

3.5. Condition optimization

In order to obtain the best electrochemical detection performance, the experimental conditions were optimized, including the incubation concentration of Ab on the interface, the reaction time between MNP-Ab and the target, and the binding time between the MNP-Ab-S1 nanocomposite and Ab on the interface. The details have been shown in the Supporting Information (Fig. S9A-F). Shortly, the following optimized conditions were found to have the best results and used in subsequent experiments: (a) the concentration of Ab: 15 μg mL^{-1}; (b) the binding time of MNP-Ab: 40 min; (c) the incubation time of MNP-Ab-S1: 40 min.

3.6. Ultra-sensitive detection of S1 protein

First, the comparative experiments between Pd-Au+Ab+*S*-MNP with the blanks (bare GCE, Pd-Au, Pd-Au+Ab) were carried out to detect S1 protein (Fig. S10), the results indicated that compared with the blanks, Pd-Au+Ab+*S*-MNP showed an observably suppressed DPV current, which proved the importance of this construction strategy. Then, the performance of the magnet-assisted electrochemical immunosensor was analyzed by DPV program under optimal conditions. Different concentrations of S1 protein in PBS were tested, and each test was performed 3 times. As shown in Fig. 5A, as the target concentration increased the DPV response at −0.074 mV gradually decreased. Fig. 5B showed the relationship between S1 protein concentration and DPV peak current. The inset showed that the current signal gradually decreased with the logarithmic value of the target concentration from 0.01 ng mL^{-1} to 1000 ng mL^{-1}, and exhibited an excellent linear relationship over a wide range ($R^2 = 0.9916$). The calibration curve was $y = 46.066 - 11.439$ lg x, where y was the peak DPV current and x was the target antigen concentration. The LOD of 0.0072 ng mL^{-1} was calculated by the signal-to-noise ratio of 3 ($S/N = 3$), according to the means of 3's blank criterion. In addition, various methods for detecting S protein and its related proteins were summarized and compared (Table S1), and the results demonstrated that this electrochemical sensor was superior to most of them. This is also due to the high catalytic performance of Pd-Au nanosheets and the signal amplification effect of MNPs. These results confirmed that this detection strategy has an excellent ability to detect S protein and can achieve ultra-sensitive detection of the target.

3.7. Repeatability and storage time stability

To evaluate the repeatability and stability of this method, multiple prepared immunosensors were stored in a dry environment at 4°C for different periods of time, and then DPV responses were tested under the same conditions (Fig. 6). The results showed that the current signals between different GCEs did not show significant
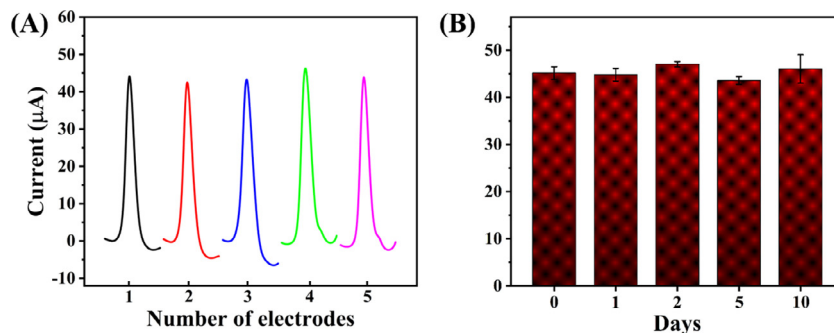
Fig. 6. (A) The reproducibility of 1 ng mL^{-1} S protein with different modified electrodes evaluated under the same conditions, (B) the storage time stability of the designed immunosensor within 10 days.
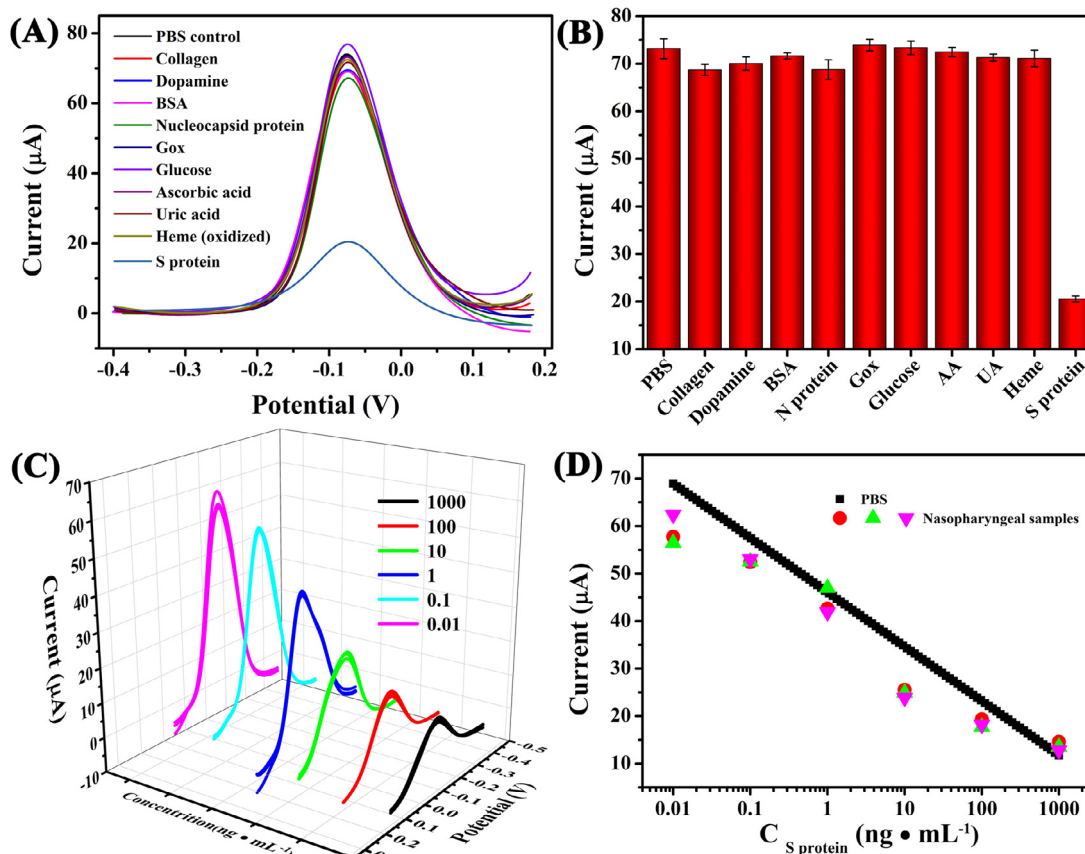

Fig. 7. (A) DPV responses after incubation with 10 proteins or molecules. (B) DPV current of electrochemical biosensor in the presence of different interferences. (C) DPV curves generated by different concentrations of S1 protein in nasopharyngeal samples ($n = 3$). (D) The dot-line graph of DPV peak current caused by S1 protein and the comparison with the standard line fitted to the PBS sample.

differences (Fig. 6A). After 10 days of storage, the electrochemical response of the modified electrode was close to its original current signal (Fig. 6B). We noticed that there is some variation in the mean valves within 10 days. Yet compare with the exiting literature, this magnet-assisted electrochemical immunosensor based on Pd-Au nanosheets has relative ultrasensitivity, simplicity, and a wide detection range [49–51].

3.8. Evaluation of selectivity and detection in nasopharyngeal samples

We evaluated the selectivity of this detection method using 10 different proteins or small molecules (Fig. 7A). The results revealed that except the S1 protein, other proteins or molecules exhibited almost constant DPV signal; and after incubating the target protein,

the current was greatly reduced (Fig. 7B). It should be pointed out that the concentration of non-target substances set was 5 times of the concentration of target substances. The above results proved that this strategy has good selectivity. In order to test the possible applications of the proposed immunoassay method, SARS-CoV-2 S1 protein was detected in the nasopharyngeal samples collected from healthy people by standard addition method. Fig. 7C showed the DPV responses caused by incubation with 5 different concentrations of S1 protein ($n = 3$), showing a gradual decrease in current signal strongly dependent on the concentration. The determination results in the complex samples were visually compared with those in PBS, and similar results were obtained (Fig. 7D). The calculated recovery rate was 84.545% - 103.520%, and the RSD was between 1.833% and 8.406% (Table S2), indicating that the feasibility of the proposed sensor for practical applications. It is important to fur-

ther validate the accuracy of the proposed sensor for future clinical samples.

Conclusion

In general, an electrochemical immunosensor was fabricated to detect SARS-CoV-2 S1 protein, achieving a LOD as low as 0.0072 ng mL^{-1} and wide detection range, which was attributed to the high conductivity, large surface-area of the surface-clean heterostructures Pd-Au nanosheets and the signal amplification and magnetic field-based transmission function of MNPs. The entire detection can be completed within 2 h The measurement results in PBS and nasopharyngeal samples proved the excellent performance of this biosensor, which can be used for early diagnosis of virus antigen. Our work presents a simple and efficient strategy to build electrochemical immunosensors based on metallic nanosheets for the sensitive detection of spike protein of SARS-CoV-2 antigen. This strategy provides meaningful ideas for the development of more rapid, economical, and mature unconventional detection methods to help medical staff predict the degree of virus infection in infected patients.

Author contributions

Jialin Zhao: Conceptualization, Data curation, Formal analysis, Writing-original draft. Zhao Fu: Formal analysis, Material preparation. Haolin Li: Formal analysis, Validation. Youlin Xiong: Data curation, Writing-review. Shuangfei Cai: Formal analysis, Conceptualization. Chen Wang: Project administration, Funding acquisition, Yunfa Chen and Ning Han: Project administration, Funding acquisition. Rong Yang: Project administration, Funding acquisition, Writing-review & editing.

Declaration of Competing Interest

The authors declare the following financial interests/personal relationships which may be considered as potential competing interests.

Acknowledgments

Supplementary materials

Supplementary material associated with this article can be found, in the online version, at doi:10.1016/j.electacta.2021.139766.

References

[1] F. Cui, H.S. Zhou, Diagnostic methods and potential portable biosensors for coronavirus disease 2019, Biosens. Bioelectron. 165 (2020) 112349.

[2] M. Yüce, E. Filiztekin, K.G. Özkaya, COVID-19 diagnosis—a review of current methods, Biosens. Bioelectron. 172 (2021) 112752.

[3] WHO Coronavirus disease (COVID-19) dashboard, https://covid19.who.int/ (accessed 2021-09-06).

[4] G. Seo, G. Lee, M.J. Kim, S.-.H. Baek, M. Choi, K.B. Ku, C.-.S. Lee, S. Jun, D. Park, H.G. Kim, S.-.J. Kim, J.-.O. Lee, B.T. Kim, E.C. Park, S.I. Kim, Rapid detection of COVID-19 causative virus (SARS-CoV-2) in human nasopharyngeal swab specimens using field-effect transistor-based biosensor, ACS Nano 14 (2020) 5135–5142.

[5] Q. Lin, D. Wen, J. Wu, L. Liu, W. Wu, X. Fang, J. Kong, Microfluidic immunoassays for sensitive and simultaneous detection of IgG/IgM/Antigen of SARS–CoV-2 within 15 min, Anal. Chem. 92 (2020) 9454–9458.

[6] M. Drobysh, A. Ramanaviciene, R. Viter, A. Ramanavicius, Affinity sensors for the diagnosis of COVID-19, Micromachines 12 (2021) 390.

[7] J. Wang, K. Cai, R. Zhang, X. He, X. Shen, J. Liu, J. Xu, F. Qiu, W. Lei, J. Wang, X. Li, Y. Gao, Y. Jiang, W. Xu, X. Ma, Novel one-step single-tube nested quantitative real-time PCR assay for highly sensitive detection of SARS-CoV-2, Anal. Chem. 92 (2020) 9399–9404.

[8] J. Dronina, U. Samukaite–Bubniene, A. Ramanavicius, Advances and insights in the diagnosis of viral infections, J. Nanobiotechnol. 19 (2021) 348.

[9] B. Udugama, P. Kadhiresan, H.N. Kozlowski, A. Malekjahani, M. Osborne, V.Y.C. Li, H. Chen, S. Mubareka, J.B. Gubbay, W.C.W. Chan, Diagnosing COVID-19: the disease and tools for detection, ACS Nano 14 (2020) 3822–3835.

[10] D.K.W. Chu, Y. Pan, S.M.S. Cheng, K.P.Y. Hui, P. Krishnan, Y. Liu, D.Y.M. Ng, C.K.C. Wan, P. Yang, Q. Wang, M. Peiris, L.L.M. Poon, Molecular diagnosis of a novel coronavirus (2019-nCoV) causing an outbreak of pneumonia, Clin. Chem. 66 (2020) 549–555.

[11] R.A.M.Safdar Khailany, M. Ozaslan, Genomic characterization of a novel SARS–CoV-2, Gene Rep. 19 (2020) 100682.

[12] Y. Bai, L. Yao, T. Wei, F. Tian, D.-.Y. Jin, L. Chen, M. Wang, Presumed asymptomatic carrier transmission of COVID-19, JAMA 323 (2020) 1406–1407.

[13] L. Zou, F. Ruan, M. Huang, L. Liang, H. Huang, Z. Hong, J. Yu, M. Kang, Y. Song, J. Xia, Q. Guo, T. Song, J. He, H.-.L. Yen, M. Peiris, J. Wu, SARS-CoV-2 viral load in upper respiratory specimens of infected patients, N. Engl. J. Med. 382 (2020) 1177–1179.

[14] F. Amanat, D. Stadlbauer, S. Strohmeier, T.H.O. Nguyen, V. Chromikova, M. McMahon, K. Jiang, G.A. Arunkumar, D. Jurczyszak, J. Polanco, M. Bermudez-Gonzalez, G. Kleiner, T. Aydillo, L. Miorin, D.S. Fierer, L.A. Lugo, E.M. Kojic, J. Stoever, S.T.H. Liu, C. Cunningham-Rundles, P.L. Felgner, T. Moran, A. García-Sastre, D. Caplivski, A.C. Cheng, K. Kedzierska, O. Vapalahti, J.M. Hepojoki, V. Simon, F. Krammer, A serological assay to detect SARS-CoV-2 seroconversion in humans, Nat. Med. 26 (2020) 1033–1036.

[15] V.M. Corman, O. Landt, M. Kaiser, R. Molenkamp, A. Meijer, D.K. Chu, T. Bleicker, S. Brünink, J. Schneider, M.L. Schmidt, D.G. Mulders, B.L. Haagmans, B. Van der, S. Veer, L. Van den Brink, G. Wijsman, J.-.L. Goderski, J. Romette, M. Ellis, M. Zambon, H. Peiris, C. Goossens, M.P. Reusken, C. Koopmans, Drosten, Detection of 2019 novel coronavirus (2019-nCoV) by real-time RT-PCR, Eurosurveillance 25 (2020) 2000045.

[16] I. Plikusiene, V. Maciulis, A. Ramanaviciene, Z. Balevicius, E. Buzavaite-Verteliene, E. Ciplys, R. Slibinskas, M. Simanavicius, A. Zvirbliene, A. Ramanavicius, Evaluation of kinetics and thermodynamics of interaction between immobilized SARS-CoV-2 nucleoprotein and specific antibodies by total internal reflection ellipsometry, J. Colloid Interface Sci. 594 (2021) 195–203.

[17] L. Zeng, Y. Li, J. Liu, L. Guo, Z. Wang, X. Xu, S. Song, C. Hao, L. Liu, M. Xin, C. Xu, Rapid, ultrasensitive and highly specific biosensor for the diagnosis of SARS-CoV-2 in clinical blood samples, Mater. Chem. Front. 4 (2020) 2000–2005.

[18] A. Wu, Y. Peng, B. Huang, X. Ding, X. Wang, P. Niu, J. Meng, Z. Zhu, Z. Zhang, J. Wang, J. Sheng, L. Quan, Z. Xia, W.Tan G. Cheng, T. Jiang, Genome composition and divergence of the novel coronavirus (2019-nCoV) originating in China, Cell Host Microbe 27 (2020) 325–328.

[19] P.C.Y. Woo, S.K.P. Lau, B.H.L. Wong, H.-.W. Tsoi, A.M.Y. Fung, R.Y.T. Kao, K.-.h. Chan, J.S.M. Peiris, K.-.y. Yuen, Differential sensitivities of severe acute respiratory syndrome (SARS) coronavirus spike polypeptide enzyme-linked immunosorbent assay (ELISA) and SARS coronavirus nucleocapsid protein ELISA for serodiagnosis of SARS coronavirus pneumonia, J. Clin. Microbiol. 43 (2005) 3054.

[20] I.S. Mahmoud, Y.B. Jarrar, W. Alshaer, S. Ismail, SARS-CoV-2 entry in host cells-multiple targets for treatment and prevention, Biochimie 175 (2020) 93–98.

[21] F.S. Felix, L. Angnes, Electrochemical immunosensors–a powerful tool for analytical applications, Biosens. Bioelectron. 102 (2018) 470–478.

[22] M.Z.H. Khan, M.R. Hasan, S.I. Hossain, M.S. Ahommed, M. Daizy, Ultrasensitive detection of pathogenic viruses with electrochemical biosensor: state of the Art, Biosens. Bioelectron. 166 (2020) 112431.

[23] R.R.X. Lim, A. Bonanni, The potential of electrochemistry for the detection of coronavirus-induced infections, Trends Anal. Chem. 133 (2020) 116081.

[24] N. Bhalla, Y. Pan, Z. Yang, A.F. Payam, Opportunities and challenges for biosensors and nanoscale analytical tools for pandemics: COVID-19, ACS Nano 14 (2020) 7783–7807.

[25] F. Shahzad, A. Iqbal, H. Kim, C.M. Koo, 2D transition metal carbides (MXenes): applications as an electrically conducting material, Adv. Mater. 32 (2020) 2002159.

[26] M. Chhowalla, H.S. Shin, G. Eda, L.-.J. Li, K.P. Loh, H. Zhang, The chemistry of two-dimensional layered transition metal dichalcogenide nanosheets, Nat. Chem. 5 (2013) 263–275.

[27] Z. Gholamvand, D. McAteer, A. Harvey, C. Backes, J.N. Coleman, Electrochemical applications of two-dimensional nanosheets: the effect of nanosheet length and thickness, Chem. Mater. 28 (2016) 2641–2651.

[28] H. Zhang, Ultrathin two-dimensional nanomaterials, ACS Nano 9 (2015) 9451–9469.

[29] L. Fabiani, M. Saroglia, G. Galatà, R. De Santis, V. Luca, G. Faggioni, N. D'Amore, E. Regalbuto, P. Salvatori, G. Terova, D. Moscone, F. Lista, F. Arduini, Magnetic beads combined with carbon black-based screen-printed electrodes for COVID-19: a reliable and miniaturized electrochemical immunosensor for SARS-CoV-2 detection in saliva, Biosens. Bioelectron. 171 (2021) 112686.

[30] C. Wang, C. Wang, X. Wang, K. Wang, Y. Zhu, Z. Rong, W. Wang, R. Xiao, S. Wang, Magnetic SERS strip for sensitive and simultaneous detection of respiratory viruses, ACS Appl. Mater. Interfaces 11 (2019) 19495–19505.

[31] K. Wu, R. Saha, D. Su, V.D. Krishna, J. Liu, M.C.J. Cheeran, J.-.P. Wang, Magnetic-nanosensor-based virus and pathogen detection strategies before and during COVID-19, ACS Appl. Nano Mater. 3 (2020) 9560–9580.

[32] K. Wu, D. Su, R. Saha, J. Liu, V.K. Chugh, J.-.P. Wang, Magnetic particle spectroscopy: a short review of applications using magnetic nanoparticles, ACS Appl. Nano Mater. 3 (2020) 4972–4989.

[33] X. Yin, X. Liu, Y.-.T. Pan, K.A. Walsh, H. Yang, Hanoi tower-like multilayered ultrathin palladium nanosheets, Nano Lett 14 (2014) 7188–7194.

[34] Y. Zhang, H. Ding, Y. Liu, S. Pan, Y. Luo, G. Li, Facile one-step synthesis of plasmonic/magnetic core/shell nanostructures and their multifunctionality, J. Mater. Chem. 22 (2012) 10779–10786.

[35] J. Zhao, D. Liang, S. Gao, X. Hu, K. Koh, H. Chen, Analyte-resolved magnetoplasmonic nanocomposite to enhance SPR signals and dual recognition strategy for detection of BNP in serum samples, Biosens. Bioelectron. 141 (2019) 111440.

[36] J. Zhao, X. Hu, X. Huang, X. Jin, K. Koh, H. Chen, A facile gold nanoparticles embeded hydrogel for non-enzymatic sensing of glucose, Colloid. Surf. B. 183 (2019) 110404.

[37] B.D. Ventura, M. Banchelli, R. Funari, A. Illiano, M.D. Angelis, P. Taroni, A. Amoresano, P. Matteini, R. Velotta, Biosensor surface functionalization by a simple photochemical immobilization of antibodies: experimental characterization by mass spectrometry and surface enhanced Raman spectroscopy, Analyst 144 (2019) 6871–6880.

[38] A. Minopoli, B.D. Ventura, B. Lenyk, F. Gentile, J.A. Tanner, A. Offenhäusser, D. Mayer, R. Velotta, Ultrasensitive antibody-aptamer plasmonic biosensor for malaria biomarker detection in whole blood, Nat. Commun. 11 (2020) 6134.

[39] R.L. Whetten, J.T. Khoury, M.M. Alvarez, S. Murthy, I. Vezmar, Z.L. Wang, P.W. Stephens, C.L. Cleveland, W.D. Luedtke, U. Landman, Nanocrystal gold molecules, Adv. Mater 8 (1996) 428–433.

[40] S. Cai, Z. Fu, W. Xiao, Y. Xiong, C. Wang, R. Yang, Zero-dimensional/two-dimensional AuxPd100–x nanocomposites with enhanced nanozyme catalysis for sensitive glucose detection, ACS Appl. Mater. Interfaces 12 (2020) 11616–11624.

[41] A. Ramanavicius, A. Finkelsteinas, H. Cesiulis, A. Ramanaviciene, Electrochemical impedance spectroscopy of polypyrrole based electrochemical immunosensor, Bioelectrochemistry 79 (2010) 11–16.

[42] F. Lima, G. Maia, Oxidized/reduced graphene nanoribbons facilitate charge transfer to the $Fe(CN)_6^{3-}/Fe(CN)_6^{4-}$ redox couple and towards oxygen reduction, Nanoscale 7 (2015) 6193–6207.

[43] Z. Zhu, J. Zhu, J. Zhao, K. Zhu, Q. Xu, H. Chen, Natural receptor-based competitive immunoelectrochemical assay for ultra-sensitive detection of Siglec 15, Biosens. Bioelectron. 151 (2020) 111950.

[44] S.J. Konopka, B. McDuffie, Diffusion coefficients of ferri-and ferrocyanide ions in aqueous media, using twin-electrode thin-layer electrochemistry, Anal. Chem. 42 (1970) 1741–1746.

[45] E. Ma, P. Wang, Q. Yang, H. Yu, F. Pei, Y. Zheng, Q. Liu, Y. Dong, Y. Li, Electrochemical immunosensors for sensitive detection of neuron-specific enolase based on small-size trimetallic Au@Pd^ Pt nanocubes functionalized on ultrathin MnO_2 nanosheets as signal labels, ACS Biomater. Sci. Eng. 6 (2020) 1418–1427.

[46] B. Hatamluyi, F. Lorestani, Z.Es haghi, Au/Pd@rGO nanocomposite decorated with poly (L-Cysteine) as a probe for simultaneous sensitive electrochemical determination of anticancer drugs, Ifosfamide and Etoposide, Biosens. Bioelectron. 120 (2018) 22–29.

[47] Q. He, J. Liu, X. Liu, G. Li, P. Deng, J. Liang, Manganese dioxide nanorods/electrochemically reduced graphene oxide nanocomposites modified electrodes for cost-effective and ultrasensitive detection of Amaranth, Colloids Surf. B 172 (2018) 565–572.

[48] X. Gao, S. Dong, L. Fu, B. Zhang, H. Hsu, G. Zou, Use of triangular silver nanoplates as low potential redox mediators for electrochemical sensing, Anal. Chem. 93 (2021) 3295–3300.

[49] J.H. Lee, M. Choi, Y. Jung, S.K. Lee, C.S. Lee, J. Kim, J. Kim, N.H. K.im, B.T. Kim, H.G. Kim, Biosens. Bioelectron. 171 (2021) 112715.

[50] Z. Fu, W. Zeng, S. Cai, H. Li, J. Ding, C. Wang, Y. Chen, N. Han, R. Yang, J. Colloid Interface Sci 604 (2021) 113–121.

[51] L. Fabiani, M. Saroglia, G. Galatà, R.D. Santis, S. Fillo, V. Luca, G. Faggioni, N.D. Amore, E. Regalbuto, P. Salvatori, G. Terova, D. Moscone, F. Lista, F. Arduini, Biosens. Bioelectron. 171 (2021) 112686.